



Cite this: *Phys. Chem. Chem. Phys.*,  
2015, 17, 2589

## Comparison of direct dynamics simulations with different electronic structure methods. $F^- + CH_3I$ with MP2 and DFT/B97-1

Rui Sun,<sup>a</sup> Collin J. Davda,<sup>ab</sup> Jiaxu Zhang<sup>c</sup> and William L. Hase<sup>\*a</sup>

In previous work, ion imaging experiments and direct chemical dynamics simulations with DFT/B97-1 were performed to study the atomic-level dynamics of the  $F^- + CH_3I \rightarrow FCH_3 + I^-$   $S_N2$  nucleophilic substitution reaction at different collision energies. Overall, the simulations are in quite good agreement with experiment at the low collision energy of 0.32 eV, however there are differences between experiment and simulation at the high collision energy of 1.53 eV. A recent CCSD(T) study of the potential energy surface for the  $F^- + CH_3I \rightarrow FCH_3 + I^-$   $S_N2$  reaction shows that it has both a traditional  $C_{3v}$  and a hydrogen-bond entrance channel. They are represented by MP2 but not by B97-1, which has only the latter channel. On the other hand, B97-1 gives a reaction exothermicity in excellent agreement with experiment, while MP2 is in error by 24.3 kJ mol<sup>-1</sup>. In the work presented here, direct dynamics simulations using MP2/aug-cc-pvdz/ECP/d were performed for the  $F^- + CH_3I \rightarrow FCH_3 + I^-$  reaction at a 1.53 eV collision energy. The same direct rebound and stripping and indirect atomistic reaction mechanisms are found in the B97-1 and MP2 simulations. Both the B97-1 and MP2 simulations agree with the experimental fraction of the available product energy partitioned to  $CH_3F$  internal energy, *i.e.*  $f_{int} = 0.59 \pm 0.08$ . However, the MP2  $f_{int}$  distribution is broader and in better agreement with experiment than B97-1. The two simulations methods give the same product energy partitioning for the stripping mechanism, but different partitionings for the rebound and indirect mechanisms. Compared to experiment, the principal difference between the B97-1 and MP2 results is the differential cross section which is nearly isotropic for B97-1. For MP2 backward scattering is more important than forward, as found in the experiments. Though there is no overall barrier for the reaction, B97-1 gives a reaction cross section appreciably larger than that for MP2, *i.e.*  $8.6 \pm 2.2 \text{ \AA}^2$  versus  $1.8 \pm 0.3 \text{ \AA}^2$ . For B97-1 59% of the reaction consists of indirect mechanisms, while for MP2 the indirect mechanisms only comprise 11% of the reaction. The experimental differential cross section is more consistent with the atomistic mechanisms for MP2 than for B97-1.

Received 12th August 2014,  
Accepted 9th October 2014

DOI: 10.1039/c4cp03589e

www.rsc.org/pccp

## 1. Introduction

Study of gas-phase  $X^- + CH_3Y \rightarrow CH_3X + Y^-$   $S_N2$  reactions is of particular interest to many experimental and theoretical chemists, for they are paradigm reactions in physical organic chemistry.<sup>1–10</sup> The traditional potential energy surface (PES) for this reaction has an ion–dipole  $X^- \cdots CH_3Y$  pre-reaction complex, a  $[X \cdots CH_3 \cdots Y]^-$  central barrier, and an ion–dipole  $XCH_3 \cdots Y^-$  post-reaction complex, all of  $C_{3v}$  symmetry.<sup>10</sup> Non-traditional (non- $C_{3v}$  symmetry) PESs are

often important; *e.g.* the  $OH^- + CH_3F$   $S_N2$  reaction with a  $CH_3OH \cdots F^-$  post-reaction complex in which  $F^-$  is hydrogen-bonded to the  $-OH$  moiety,<sup>11</sup> and the  $F^- + CH_3I$  reaction with a hydrogen-bonded  $F^- \cdots HCH_2I$  pre-reaction complex.<sup>12</sup>

In previous work Zhang *et al.*<sup>12</sup> investigated the PES for the  $F^- + CH_3I \rightarrow FCH_3 + I^-$   $S_N2$  reaction with different electronic structure theories and basis sets. Of particular interest is that MP2<sup>13</sup> and DFT<sup>14</sup> give different entrance-channel PESs for this reaction, as shown in Fig. 1. For the DFT/B97-1 PES there are only a hydrogen-bonded  $F^- \cdots HCH_2I$  pre-reaction complex and a hydrogen-bonded  $[F \cdots HCH_2 \cdots I]^-$  transition state (TS). In contrast, the MP2 PES has these stationary point structures as well as the traditional  $F^- \cdots CH_3I$  ion–dipole complex and  $[F \cdots CH_3 \cdots I]^-$  TS, both with  $C_{3v}$  symmetry. The DFT functionals OPBE,<sup>15</sup> OLYP,<sup>16</sup> HCTH407,<sup>17</sup> and BhandH,<sup>18</sup> give PESs similar to the B97-1 PES in Fig. 1, and only BhandH with a triple-zeta basis set

<sup>a</sup> Department of Chemistry and Biochemistry, Texas Tech University, Lubbock, Texas 79409-1061, USA. E-mail: bill.hase@ttu.edu

<sup>b</sup> Trinity Valley School, Fort Worth, Texas 76132-4553, USA

<sup>c</sup> Institute of Theoretical and Simulation Chemistry, Academy of Fundamental and Interdisciplinary Sciences, Harbin Institute of Technology, Harbin 150080, P. R. China

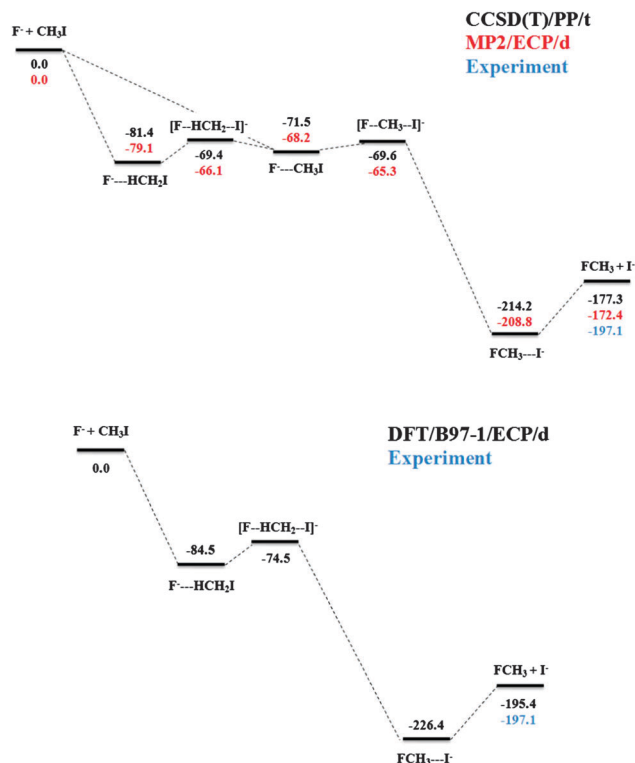


Fig. 1 Critical points on the potential energy surface for the  $F^- + CH_3I \rightarrow FCH_3 + I^-$   $S_N2$  reaction: (a) CCSD(T)/PP/t (black), MP2/ECP/d (red), and experiment (blue); (b) DFT/B97-1 (black) and experiment (blue). The potential energies ( $\text{kJ mol}^{-1}$ ) are classical energies without zero point energy. The DFT/B97-1 results were presented previously.<sup>19,20</sup>

gives traditional entrance-channel  $C_{3v}$  stationary points similar to those for the MP2 PES.<sup>12</sup>

The DFT/B97-1/ECP/d level of theory was chosen for the previous direct dynamics simulations<sup>19,20</sup> of the  $F^- + CH_3I$  reaction, since it gives a heat of reaction in excellent agreement with experiment. The simulations were performed at collision energies at 0.32 and 1.53 eV, and overall quite good agreement was found with experiment; *e.g.* the experimental and simulation average fractions of product energy partitioning are statistically the same. However, for the higher energy 1.53 eV collisions differences were found between the experimental and simulation dynamics.<sup>20</sup> The internal energy distribution of the  $CH_3F$  product is narrower in the simulations than in the experiments, and the product scattering angle distribution is nearly isotropic in the simulations, but has an important backward scattering component in the experiments.

Recently, Sun *et al.*<sup>21</sup> performed CCSD(T)<sup>22</sup> single point optimization calculations with different basis sets to assess the accuracy of the MP2 and DFT PESs for the  $F^- + CH_3I \rightarrow FCH_3 + I^-$  entrance-channel stationary points. Similar to the MP2 PES, both the hydrogen-bonded and traditional  $C_{3v}$  stationary points were found for the CCSD(T) PES with all basis sets considered. The energetics for the CCSD(T)/PP/t PES are depicted in Fig. 1 and the other basis sets give a similar result; *i.e.* all of the basis set used for the CCSD(T) calculations are described below as well as in ref. 12 and 21. These CCSD(T) calculations strongly

suggest that the  $F^- + CH_3I$  entrance-channel has  $C_{3v}$  stationary points as found for the MP2 PES, which are absent in PESs determined from all of the DFT calculations except one.<sup>12</sup>

In the work presented here MP2/ECP/d direct dynamics simulations were performed to investigate the possibility that the differences in the MP2 and B97-1 PESs affect the reaction dynamics. Interestingly, B97-1 gives reactive scattering dynamics at 0.32 eV which are in good agreement with experiment and the differences are found at the higher collision energy of 1.53 eV.<sup>19,20</sup> Accordingly, the MP2 simulations were performed for this latter energy to compare the results with experimental data as well as the previous simulations using B97-1/ECP/d.<sup>20</sup> Section II describes the computational methodology for both the *ab initio* calculations and direct dynamics simulations, and the results of the simulations are presented in Section III. Differences between the MP2 and DFT simulation results are discussed in Section IV. The article ends with a Summary in Section V.

## II. Computational methodology

### A. *Ab initio* calculations

The MP2/ECP/d method was used for the direct dynamics simulations. Detailed discussions of different electronic structure calculations for the  $F^- + CH_3I \rightarrow FCH_3 + I^-$  PES are discussed elsewhere<sup>12,21</sup> and briefly presented here. The ECP/d basis set is a combination of: the Wadt and Hay effective core potential (ECP)<sup>23</sup> for the core electrons; Dunning and Woon's aug-cc-pVDZ basis set<sup>24,25</sup> for the C, H, and F atoms; and for iodine a 3s, 3p basis set for the valence electrons, augmented by a d-polarization function with a 0.262 exponent, and s, p, and d diffuse functions with exponents of 0.034, 0.039, and 0.0873.<sup>26</sup> The PP/t basis set consists of the aug-cc-pVTZ basis set<sup>24,25</sup> for the C, H, and F atoms, and Peterson's aug-cc-pVTZ basis set, with a pseudopotential (PP) for iodine.<sup>27</sup>

Similar to the CCSD(T)/PP/t PES shown in Fig. 1, the MP2/ECP/d PES has both the traditional  $C_{3v}$  and hydrogen-bonded entrance channels, with the respective  $[F\cdots CH_3\cdots I]^-$  and  $[F\cdots HCH_2\cdots I]^-$  TSs. Intrinsic reaction coordinate (IRC)<sup>28</sup> calculations were performed to understand the connectivity of the  $C_{3v}$  and hydrogen-bonded stationary points for the MP2 PES.<sup>12</sup> The hydrogen-bonded TS is connected with both the hydrogen-bonded and  $C_{3v}$  pre-reaction complexes. The  $C_{3v}$  TS is connected with the  $C_{3v}$  pre- and post-reaction complexes.

For the MP2/ECP/d PES, the classical potential energy difference between the  $F\cdots CH_3I$  pre-reaction complex and  $[F\cdots CH_3\cdots I]^-$  TS for the  $C_{3v}$  pathway is  $2.9 \text{ kJ mol}^{-1}$ , and  $13.0 \text{ kJ mol}^{-1}$  between the  $F\cdots HCH_2I$  pre-reaction complex and  $[F\cdots HCH_2\cdots I]^-$  TS for the hydrogen-bonded pathway. The corresponding CCSD(T)/PP/t energies are  $1.9 \text{ kJ mol}^{-1}$  and  $12.0 \text{ kJ mol}^{-1}$ . The respective classical potential energy release values from the  $F^- + CH_3I$  separated reactants to the  $F\cdots CH_3I$   $C_{3v}$  complex and to the  $F\cdots HCH_2I$  hydrogen-bonded complex are  $68.2$  and  $79.1 \text{ kJ mol}^{-1}$  for MP2/ECP/d, compared to  $71.5$  and  $81.4 \text{ kJ mol}^{-1}$  for CCSD(T)/PP/t. Stationary point geometries are given in Table 2 of ref. 21,

and MP2/ECP/d gives structures very similar to those for CCSD(T)/PP/t. As a result of these comparisons between CCSD(T) and MP2, MP2/ECP/d was chosen as the electronic structure method for direct dynamics simulations to investigate the effect of the “additional”  $C_{3v}$  entrance channel pathway compared to the previous DFT simulations.<sup>19,20</sup>

The energies in Fig. 1 are classical potential energies and, if harmonic zero-point energy (zpe) is included, the energies ( $\text{kJ mol}^{-1}$ ) for the stationary points with respect to  $\text{F}^- + \text{CH}_3\text{I}$  are:  $\text{F}^- \cdots \text{HCH}_2\text{I}$ ,  $-79.5$ ;  $[\text{F}^- \cdots \text{HCH}_2 \cdots \text{I}]^-$ ,  $-66.1$ ;  $\text{F}^- \cdots \text{CH}_3\text{I}$ ,  $-67.4$ ;  $[\text{F}^- \cdots \text{CH}_3 \cdots \text{I}]^-$ ,  $-64.4$ ;  $\text{FCH}_3 \cdots \text{I}^-$ ,  $-200.4$ ; and  $\text{FCH}_3 + \text{I}^-$ ,  $-164.8$ . These energies with zpe included are similar to the classical potential energies, except for the post-reaction complex and products. For these two stationary points, the  $\text{CH}_3\text{F}$  vibrational frequencies are substantially different from those for the reactant  $\text{CH}_3\text{I}$ .

### B. Direct dynamics simulations

Classical trajectory simulations have been widely used to study chemical dynamics since the early 1960's.<sup>29</sup> They provide important atomic-level information such as reaction pathways,<sup>30</sup> rate constants,<sup>31</sup> and intramolecular vibrational energy redistribution (IVR) rates.<sup>32</sup> A broadly applicable approach for performing these simulations is Born–Oppenheimer direct dynamics<sup>33–35</sup> for which the potential energy and its gradient, needed to numerically solve the classical equations of motion, are obtained directly from an electronic structure theory. An enhancement in the simulation efficiency is to use the molecular orbitals (MOs) obtained from the previous integration step to initiate the self-consistent field<sup>36</sup> (SCF) procedure for the current integration step. This approach ensures the trajectory remains on the same adiabatic electronic state, since the MOs for the previous step are expected to have the same character as those for the current integration step. The direct dynamics simulations presented here were performed with the VENUS/NWChem<sup>37</sup> software package, which has tight coupling between the classical dynamics simulation code VENUS<sup>38,39</sup> and the electronic structure code NWChem.<sup>40</sup>

### C. Trajectory initial conditions and calculations

For the best accuracy and computational cost, the trajectory integrations were performed with the velocity-Verlet<sup>41</sup> method using a time step is 0.2 fs. The trajectories were integrated for a maximum time of 5 ps, or until the distance between C–I or C–F exceeded 15 Å, which was considered to be formation of products or reactants, respectively. Initial conditions for the simulations were chosen to be identical with the experiments to compare simulation and experiment. Quasiclassical sampling<sup>42</sup> was used to select initial conditions for  $\text{CH}_3\text{I}$  with 360 K and 75 K vibrational and rotational temperatures, respectively. The  $\text{CH}_3\text{I}$  molecule was randomly rotated about its Euler angles. The  $\text{F}^- + \text{CH}_3\text{I}$  collision energy is fixed at 1.53 eV with an initial separation of 15 Å. Different impact parameters were chosen for the collision as described below.

Before presenting the results of the simulations, it is important to assess the accuracy of classical dynamics for the  $\text{F}^- + \text{CH}_3\text{I} \rightarrow \text{CH}_3\text{F} + \text{I}^-$   $S_{\text{N}}2$  reaction. Classical dynamics do not preserve zpe

constraints,<sup>43</sup> and bimolecular<sup>44,45</sup> and unimolecular<sup>46</sup> reactions can occur classically without zpe in the modes orthogonal to the reaction coordinate as the reactive system passes the TS. Thus, if tunneling is unimportant, the classical threshold for reaction will be less than that for quantum dynamics. For intramolecular vibrational energy redistribution (IVR),<sup>32</sup> classical dynamics may allow zpe to unphysically flow from a mode and enhance the rate of IVR.<sup>47,48</sup>

The neglect of zpe constraints in classical dynamics becomes important when the energy of the reactive system is in only slight excess of its zero point energy. Fortunately, as a result of the high collision energy of 1.53 eV and the large exothermicity in forming the pre-reaction complex and reaction products, problems with zpe are unexpected for the  $\text{F}^- + \text{CH}_3\text{I} \rightarrow \text{CH}_3\text{F} + \text{I}^-$   $S_{\text{N}}2$  reaction. The reactive system is expected to have zpe when crossing the TS, separating the pre-reaction complex and products, and when forming the products. Thus, classical dynamics is expected to be accurate for the  $\text{F}^- + \text{CH}_3\text{I} \rightarrow \text{CH}_3\text{F} + \text{I}^-$   $S_{\text{N}}2$  reaction at a collision energy of 1.53 eV, and any differences between the classical dynamics simulations and experiment are expected to result from shortcomings in the PES.

## III. MP2 simulation results

### A. Microscopic reaction mechanisms, reaction probabilities, and cross sections

The reaction dynamics were studied by calculating ensembles of trajectories at fixed values of impact parameter  $b$ . To identify the largest impact parameter at which reaction occurs,  $b_{\text{max}}$ , 200 trajectories were calculated for each  $b$  of 4.75, 5.00, 5.25, 5.50, 5.75, 6.00 Å. For this range of  $b$ , reaction was observed at only  $b$  of 4.75 Å and not at the higher  $b$ . Therefore, 4.75 Å was identified as  $b_{\text{max}}$  and subsequent trajectories were sampled with  $b$  less than this  $b_{\text{max}}$ , and 500 trajectories were calculated for each of  $b$  of 0, 1, 2, 3, 4, and 4.75 Å. Two reaction pathways were observed, *i.e.*  $S_{\text{N}}2$  nucleophilic substitution  $\text{F}^- + \text{CH}_3\text{I} \rightarrow \text{FCH}_3 + \text{I}^-$  and proton transfer  $\text{F}^- + \text{CH}_3\text{I} \rightarrow \text{HF} + \text{CH}_2\text{I}^-$ . The research discussed here focuses on the  $S_{\text{N}}2$  reaction and the dynamics of proton transfer will be considered in the future.

The  $S_{\text{N}}2$  reaction probability *versus* impact parameter is shown in Fig. 2. Even though the reaction has no overall barrier, the simulations still predict a very low reaction probability, *i.e.* less than 12% for each impact parameter, which decreases as the impact parameter increases. Similar to what has been observed for other  $S_{\text{N}}2$  reactions,<sup>19,20,49</sup> the reaction occurs by two direct atomic-level mechanisms, *i.e.* rebound and stripping, and different types of indirect mechanisms. For the direct rebound mechanism  $\text{F}^-$  directly attacks the backside of  $\text{CH}_3\text{I}$ , rebounds backward off the massive I-atom, and forms a highly excited C–F bond in  $\text{CH}_3\text{F}$  molecule. The stripping direct reaction mechanism occurs when  $\text{F}^-$  approaches the side of the methyl iodide molecule and strips the methyl group away from the I-atom, with  $\text{CH}_3\text{F}$  scattering in the forward direction. This reaction mechanism gives the newly formed  $\text{CH}_3\text{F}$  molecule an

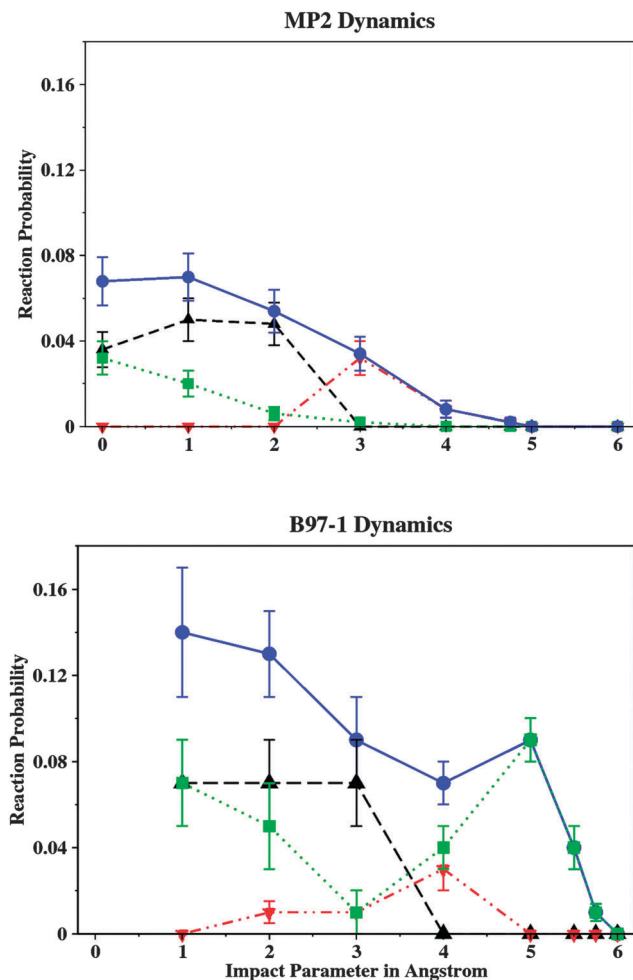


Fig. 2 Reaction probabilities,  $P_r(b)$ , for the  $F^- + CH_3I$   $S_N2$  reaction versus impact parameter: MP2 dynamics top graph and DFT/B97-1 dynamics bottom graph. The lines are for the total  $S_N2$  (blue solid line with circle), direct rebound (black dash line with upper triangle), direct stripping (red dash line with down triangle), and indirect (green dash line with square) reactions. The DFT/B97-1 results were presented previously.<sup>19,20</sup>

increased amount of rotational energy. Depictions of the rebound and stripping mechanisms are given in a previous article describing  $F^- + CH_3I$   $S_N2$  dynamics.<sup>19</sup>

The indirect reaction is more complicated and occurs by multiple mechanisms including formation of the pre-reaction complex (A) or post-reaction complex (B), the roundabout mechanism (Ra),<sup>50</sup> barrier recrossing (br),<sup>51,52</sup> and combinations of these processes. For complex formation, one or both of the pre-reaction complexes  $F^- \cdots CH_3I$  and  $F^- \cdots HCH_2I$  and/or post-reaction complex  $FCH_3 \cdots I^-$  have multiple vibrations between the anion and the molecular moiety, resulting in a lifetime that is observable in the atomic animations. Barrier recrossing was first observed for  $S_N2$  reactions in  $Cl^- + CH_3Cl$  central barrier dynamics.<sup>51</sup> For the roundabout mechanism,  $F^-$  first strikes the  $CH_3$  group on its side, causing it to rotate one or more times around the massive I atom. Then, after one or more  $CH_3$  revolutions,  $F^-$  attacks the C atom backside and directly displaces  $I^-$ . This reaction mechanism has been discussed in detail previously.<sup>50</sup>

Percentages for the different indirect mechanisms are complex formation (42%), barrier recrossing (32%), roundabout (16%), and barrier recrossing + complex formation (10%).

As reported for other  $S_N2$  reactions<sup>19,20,49</sup> and shown in Fig. 2, the probabilities of the atomistic mechanisms are heavily dependent on  $b$ . Direct rebound is the most likely mechanism at small  $b$ , for which the incoming fluoride ion attacks carbon backside. Direct stripping replaces direct rebound as the most probable mechanism at larger  $b$ . The probability of the indirect mechanism decreases near linearly as  $b$  increases. The reaction cross section  $\sigma_r$  is obtained by integrating the reaction probability versus  $b$ ,  $P_r(b)$ , over  $b$ ; *i.e.*  $\sigma_r = 2\pi \int P_r(b)b db$ . The total reaction cross section is  $1.8 \pm 0.3 \text{ \AA}^2$ , and those for the direct rebound, direct stripping, and indirect mechanisms are  $0.8 \pm 0.3 \text{ \AA}^2$ ,  $0.8 \pm 0.2 \text{ \AA}^2$ ,  $0.2 \pm 0.06 \text{ \AA}^2$ , respectively. The rebound, stripping, and indirect percentages of the reaction are 46, 43, and 11%, respectively.

## B. Product energy partitioning

The average  $I^- + CH_3F$  product energy partitioning for the current MP2/ECP/d simulations are given in Table 1. The overall fraction partitioned to  $CH_3F$  rotation + vibration is  $0.66 \pm 0.01$  from MP2/ECP/d, statistically the same as the experimental result of  $0.59 \pm 0.08$ .

Fig. 3 presents the distribution of the  $CH_3F$  internal energy, obtained from the MP2 simulations, which is compared with the experimental distribution. The two distributions are similar, in that both have the same upper bound of  $\sim 3.4$  eV.<sup>20</sup> Both distributions have the same most probable internal energy of 2.4 eV and also similar shapes in the vicinity of the distributions' peaks. The experimental data contains a more diffuse lower bound in the distribution, due to the finite energy resolution,<sup>20</sup> which is not present in the MP2 simulations. Overall the MP2/ECP/d internal energy distribution for  $CH_3F$  is in agreement with experiment.

Table 1 Average fractions of  $F^- + CH_3I \rightarrow CH_3F + I^-$  product energy partitioning<sup>a</sup>

	$f_{rot}$	$f_{vib}$	$f_{rel}$	$f_{int}$
DFT/B97-1 <sup>b</sup>				
Direct rebound	$0.19 \pm 0.03$	$0.27 \pm 0.04$	$0.54 \pm 0.03$	$0.46 \pm 0.03$
Direct stripping	$0.27 \pm 0.03$	$0.45 \pm 0.04$	$0.28 \pm 0.02$	$0.72 \pm 0.02$
Indirect	$0.07 \pm 0.03$	$0.62 \pm 0.04$	$0.31 \pm 0.02$	$0.69 \pm 0.02$
Total	$0.12 \pm 0.03$	$0.51 \pm 0.06$	$0.37 \pm 0.04$	$0.63 \pm 0.04$
MP2				
Direct rebound	$0.07 \pm 0.01$	$0.56 \pm 0.02$	$0.37 \pm 0.02$	$0.63 \pm 0.02$
Direct stripping	$0.21 \pm 0.02$	$0.45 \pm 0.01$	$0.34 \pm 0.01$	$0.66 \pm 0.02$
Indirect	$0.14 \pm 0.05$	$0.71 \pm 0.07$	$0.15 \pm 0.03$	$0.85 \pm 0.07$
Total	$0.13 \pm 0.01$	$0.53 \pm 0.01$	$0.34 \pm 0.01$	$0.66 \pm 0.01$
Experiment <sup>b</sup>				
Total				$0.59 \pm 0.08$

<sup>a</sup> The  $f$ 's are fractions of energy partitioned to rotational, vibrational, relative translational, and internal (rotation + vibration) energy. Total is the combined partitioning for the mechanisms. <sup>b</sup> Data obtained from Table 2 of ref. 20.

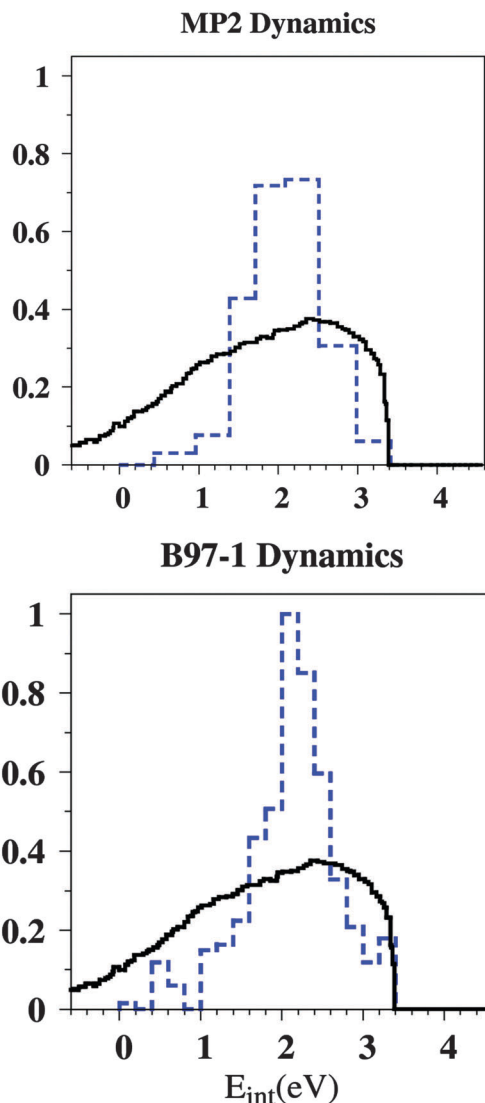


Fig. 3 Normalized histogram distributions of the  $\text{CH}_3\text{F}$  internal (rotation + vibration) energy for the MP2 and B97-1 simulations. The black solid curve is the experimental result and the blue dash curve is from simulation. The DFT/B97-1 results were presented previously.<sup>19,20</sup>

### C. Center-of-mass velocity scattering angle

The scattering angle  $\theta$ , between the reactant and product ion relative velocity vectors,<sup>50</sup> was calculated for each reactive trajectory. The resulting distribution of this angle includes all values within the  $2\pi$  solid angle, whose area is proportional to  $\sin \theta$ , and a comparison may be made with experiment.<sup>20,50</sup> The experiments only determine the relative intensity of the scattering versus  $\theta$ ,<sup>20,50</sup> and the experimental and simulation relative scattering intensities are compared here.

Fig. 4 presents the histogram of the cosine of the scattering angle  $\theta$  for the total  $\text{S}_{\text{N}}2$  reaction and Fig. 5 presents the histograms for the rebound, stripping, and indirect atomistic mechanisms. The direct rebound mechanism leads to a backward scattering with  $\cos \theta$  negative, as the  $\text{CH}_3\text{F}$  product fluorine bounces off the much more massive iodine atom. Though the direct stripping mechanism leads to forward scattering with

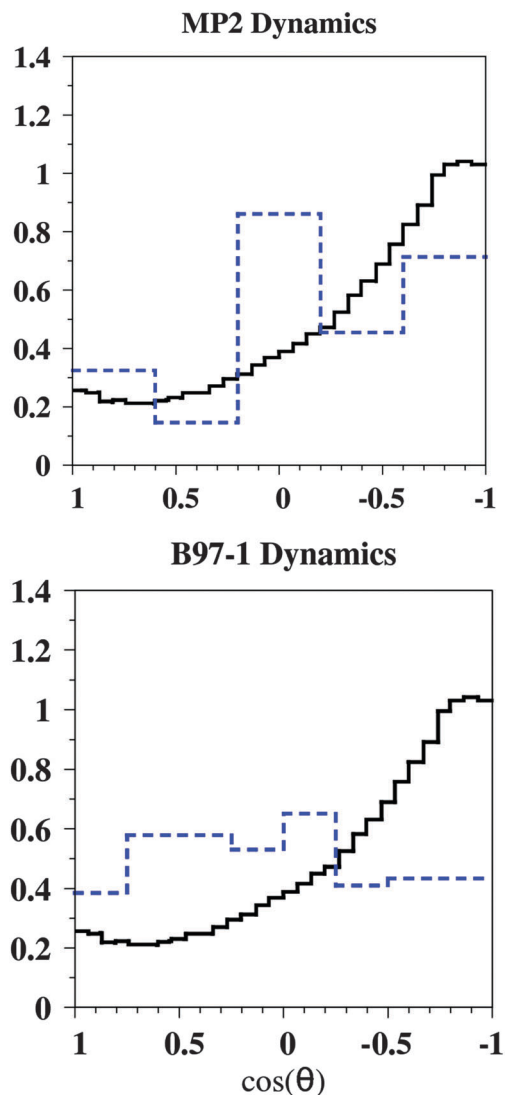


Fig. 4 Normalized histogram distributions of the velocity scattering angle distribution for the  $\text{F}^- + \text{CH}_3\text{I} \rightarrow \text{FCH}_3 + \text{I}^-$   $\text{S}_{\text{N}}2$  reaction. The results for both the MP2 and B97-1 simulations are presented in the blue dash curves. The black solid curve is the experimental result. Negative and positive  $\cos(\theta)$  correspond to backward and forward scattering, respectively. The DFT/B97-1 results were presented previously.<sup>19,20</sup>

$\cos \theta$  positive, a large fraction of the direct stripping trajectories have scattering with the cosine value close to zero (see previous discussion in ref. 19 and 20). Isotropic scattering is observed for the combined indirect mechanisms, as found in previous studies.<sup>19,20,49</sup> For the total reaction, there is good agreement between the experimental scattering angle distribution<sup>20</sup> and the scattering distribution determined from the MP2 simulations, particularly for the forward and backward regions. However, the simulations predict a large portion of the scattering with  $\cos \theta$  close to zero, which is absent in the experiments.<sup>20</sup> It is of interest that almost all of the “sideways” scattered trajectories, with  $\cos \theta$  close to zero, are from the ensemble with an impact parameter  $b$  of 3 Å, with very few coming from the ensembles with  $b$  of 1 and 2 Å. Thus, it is possible that this sideways scattering would not be as pronounced if  $b$  was sampled

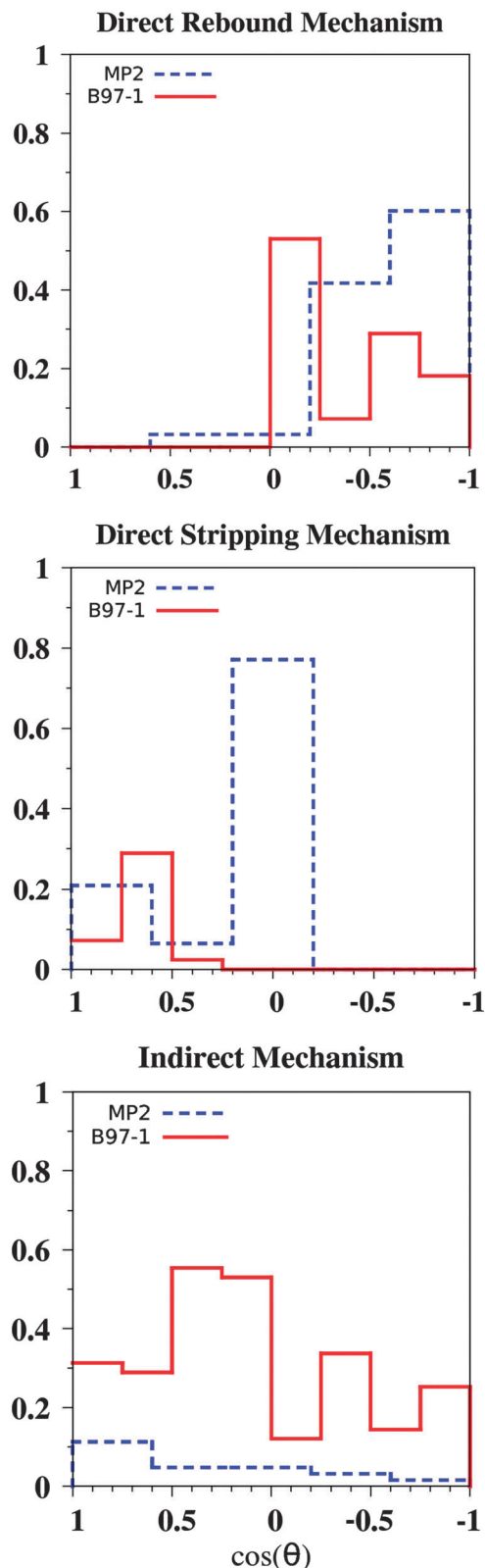


Fig. 5 Velocity scattering angle distributions from MP2 (blue dash) and B97-1 (red solid) for the rebound, stripping, and indirect mechanisms. The sum of the individual distributions is normalized to unity. The area of each distribution is proportional to its contribution to the atomistic dynamics. The DFT/B97-1 results were presented previously.<sup>19,20</sup>

continuously between 0 and  $b_{\max}$  for the simulations.<sup>42</sup> Nevertheless, the MP2 scattering angle distribution is dominated by backward scattering and in overall agreement with experiment.

## IV. Comparison of MP2 and DFT/B97-1 direct dynamics

In the following, the MP2 simulation results reported above are compared with the previous B97-1 results.<sup>19,20</sup>

### A. Reaction probabilities and cross sections

The MP2 and B97-1 total  $S_{N2}$  reaction probabilities *versus* impact parameter,  $P_r(b)$ , are compared in Fig. 2. The B97-1  $P_r(b)$  are approximately a factor of two larger than the MP2 values and, in addition,  $P_r(b)$  extends to  $\sim 6$  Å for B97-1 but only to  $\sim 5$  Å for MP2. As a result, the B97-1  $S_{N2}$  reaction cross section is appreciably higher than the MP2 value and is  $8.6 \pm 2.2$  Å<sup>2</sup>, as compared to  $1.8 \pm 0.3$  Å<sup>2</sup> for MP2. This difference in the MP2 and B97-1 reactive cross sections probably arises from multiple factors. One is the broader range of impact parameters leading to reaction for the B97-1 dynamics. Another is that for MP2 the TS connecting the pre-reaction complex to the products is  $\sim 10$  kJ mol<sup>-1</sup> higher in energy (see Fig. 1).

As shown in Fig. 2, the MP2 and B97-1 dynamics have the same direct rebound, direct stripping, and indirect atomistic mechanisms. The overall characteristics of the MP2 and B97-1  $P_r(b)$  are similar for the rebound and stripping mechanisms, with the proviso that the rebound  $P_r(b)$  are larger for the B97-1 calculations. The striking difference between the MP2 and B97-1 dynamics is for the indirect mechanism, whose B97-1 probability peaks at large impact parameters. For the  $b = 0-3$  Å range, the  $P_r(b)$  for MP2 and B97-1 are similar, but for the larger  $b$  B97-1 has a much higher probability for the indirect mechanism. The B97-1 cross sections for the rebound, stripping, and indirect mechanisms are  $2.5 \pm 0.7$ ,  $1.0 \pm 0.3$ , and  $5.1 \pm 1.7$  Å<sup>2</sup>, respectively, which give respective probabilities of 29, 12, and 59%, respectively. The MP2 cross sections for the rebound, stripping, and indirect mechanisms are  $0.8 \pm 0.3$  Å<sup>2</sup>,  $0.8 \pm 0.2$  Å<sup>2</sup>, and  $0.2 \pm 0.06$  Å<sup>2</sup>, respectively, resulting in respective percentages of 46, 43, and 11%. Thus, the indirect mechanism is dominant (59%) for the B97-1 dynamics, but a minor contributor (11%) for MP2. The B97-1 cross section for the rebound mechanism is four times larger than the MP2 value, while the B97-1 and MP2 cross sections are the same for the stripping mechanism.

### B. Product energy partitioning

The average product energy partitioning fractions for the DFT/B97-1 and MP2 simulations are summarized in Table 1. The overall DFT/B97-1 and MP2 fractions partitioned to CH<sub>3</sub>F internal excitation,  $f_{\text{int}}$ , are  $0.63 \pm 0.04$  and  $0.66 \pm 0.01$ , respectively, and statistically the same as the experimental result of  $0.59 \pm 0.08$ . In addition, the partitionings to  $f_{\text{rot}}$ ,  $f_{\text{vib}}$ , and  $f_{\text{rel}}$  are also the same for B97-1 and MP2.

Differences in the energy partitioning are apparent for the atomic-level rebound and indirect mechanisms. The B97-1 and

MP2 energy partitionings are similar for the stripping mechanism. For the rebound mechanism, B97-1 preferentially transfers energy to product relative translation (0.54), while the majority of the transfer is to CH<sub>3</sub>F vibration (0.56) with MP2. Correspondingly,  $f_{\text{int}}$  is 0.46 for B97-1 and 0.63 for MP2. For the indirect reaction,  $f_{\text{rel}}$  for MP2 is one-half that for B97-1. As a result,  $f_{\text{int}}$  is 0.85 and 0.69 for MP2 and B97-1, respectively.

The CH<sub>3</sub>F internal energy distributions, from the B97-1 and MP2 simulations, are compared in Fig. 3. Both B97-1 and MP2 have the same high energy cut-off, but overestimate the distribution in the region of approximately 1.5–2.5 eV. Both B97-1 and MP2 do not capture the low energy region of the distribution as compared to experiment.<sup>20</sup> However, there is some experimental uncertainty for this region due to diffuseness in the data and, resulting, finite energy resolution.<sup>20</sup> The most probable energy of 2.4 eV from the MP2 simulations is similar but slightly larger than the B97-1 value of 2.2 eV. Overall, the MP2 internal energy distribution is broader and in better agreement with experiment than B97-1.

### C. Center-of-mass velocity scattering angle

The MP2 and B97-1 center-of-mass velocity scattering angle distributions are given in Fig. 4, where they are compared with experiment. Experiment is dominated by backward scattering, but B97-1 predicts almost isotropic scattering. The MP2 scattering angle distribution agrees well with experiment, except for a surprisingly large probability of sideways scattering, that is discussed in Section III.C. Overall, the MP2 simulations reproduce the backward scattering observed in the experiments. This is a result of less indirect reaction in MP2 as compared to the B97-1 simulations and the, resulting, more important rebound mechanism for the MP2 simulations.

The MP2 velocity scattering angle distributions for the rebound, stripping, and indirect mechanisms are compared in Fig. 5, and their characteristics are similar to what was found for the previous B97-1 simulations. Rebound is backward scattering, stripping forward, and indirect overall isotropic. What is different between the MP2 and B97-1 scattering is the sideways component in the MP2 stripping, which is not present for B97-1.

## V. Summary

In the work presented here MP2/ECP/d direct dynamics for the  $\text{F}^- + \text{CH}_3\text{I} \rightarrow \text{CH}_3\text{F} + \text{I}^-$  S<sub>N</sub>2 reaction, at a collision energy of 1.53 eV, are compared with those presented previously using the B97-1/ECP/d method.<sup>19,20</sup> There are differences between the B97-1 and experimental results for this collision energy. Comparisons are often made between different electronic structure methods in calculating stationary point properties such as structures, vibrational frequencies, and energies, and it is important to understand how the reaction dynamics depend on the level of electronic structure theory used in direct dynamics simulations. The work presented here addresses this subject.

There are differences in the entrance channel for the MP2 and B97-1 PESs.<sup>12</sup> As shown in Fig. 1, for B97-1 there is only the

hydrogen-bonded pathway, while for MP2 there is this pathway and the traditional C<sub>3v</sub> pathway. The MP2 PES agrees with higher level CCSD(T) calculations,<sup>21</sup> which is expected to be accurate. The effect of such an inaccuracy in the reaction pathways for the B97-1 PES might be expected to be most pronounced at low energy. However, interestingly, B97-1 gives overall dynamics which agree with experiment at the low collision energy of 0.32 eV.<sup>19,20</sup> It is at the higher collision energy of 1.53 eV where there are differences between the B97-1 dynamics and experiment. This is the energy considered here.

MP2 and B97-1 give the same atomistic direct rebound, direct stripping, and indirect atomistic mechanisms for the  $\text{F}^- + \text{CH}_3\text{I} \rightarrow \text{CH}_3\text{F} + \text{I}^-$  S<sub>N</sub>2 reaction, but these theories differ in the relative importance of these mechanisms and in the total reaction cross section. The major difference for the atomistic mechanisms is that B97-1 predicts that 59% of the reaction is indirect, while only 11% for MP2. In addition, the rebound mechanism is more important for the MP2 dynamics. A property which conceivably could be determined by experiment is the S<sub>N</sub>2 reaction cross section, for which the B97-1 and MP2 values are  $8.6 \pm 2.2$  and  $1.8 \pm 0.3$  Å<sup>2</sup>, respectively. Experiment could identify which is more accurate, which may provide insight to whether MP2 or B97-1 more accurately describes the atomic-level mechanisms. It is noteworthy that the experimental scattering is characterized by nearly equal isotropic and backward scattered components, indicating an appreciable indirect component in the scattering dynamics.<sup>20</sup>

Both B97-1 and MP2 give an average energy partitioning to CH<sub>3</sub>F internal energy which is in agreement with experiment. However, the MP2 distribution for this energy is in somewhat better agreement with experiment than found from the B97-1 simulations, but there is some uncertainty in the exact form of the experimental distribution.<sup>20</sup> The stripping mechanism gives similar energy partitioning for the MP2 and B97-1 simulations, but the energy partitioning is different for the rebound and indirect mechanisms. For MP2 the majority of the rebound energy partitioning is to CH<sub>3</sub>F vibration, but for B97-1 it is to relative translation. For the indirect mechanism, MP2 partitions 0.85 of the available energy to CH<sub>3</sub>F internal energy and, in contrast, this fraction is 0.69 for B97-1. These are interesting differences in the atomistic product energy partitioning, which are difficult to determine experimentally. For example, the rebound mechanism has backward scattering, but this scattering is convoluted with that for the indirect mechanism which also has a backward component.

The MP2 differential cross section is in much better agreement with experiment than found from the B97-1 simulations. There is a large backward (*i.e.* rebound) component in the experimental scattering and B97-1 does not give this. Instead, these simulations give a near isotropic scattering distribution.

The above comparisons between experiment and the MP2 and B97-1 simulations, at a collision energy of 1.53 eV, suggest the former may be more accurate. However, more experimental information is needed, *e.g.* the S<sub>N</sub>2 reaction cross section. For the 12-dimensional 6-atom  $\text{F}^- + \text{CH}_3\text{I} \rightarrow \text{CH}_3\text{F} + \text{I}^-$  reaction, it is difficult to quantify which differences in the MP2 and B97-1

PESs affect the 1.53 eV reaction dynamics. The B97-1 PES has a classical heat of reaction of  $-195.4 \text{ kJ mol}^{-1}$  which is in excellent agreement with the experimental value of  $-196.7 \text{ kJ mol}^{-1}$ , while that for MP2 is  $-172.4 \text{ kJ mol}^{-1}$  and in error by  $24.3 \text{ kJ mol}^{-1}$ .<sup>21</sup> In addition, direct dynamics simulations for the  $\text{OH}^- + \text{CH}_3\text{I}$  reaction, with B97-1, give rate constants in excellent agreement with experiment.<sup>53</sup> On the other hand, CCSD(T) calculations<sup>21</sup> indicate that MP2 more accurately describes the entrance channel reaction paths for the  $\text{S}_{\text{N}}2$  reaction. The MP2 barrier, for the TS connecting the pre-reaction complex with products, is  $\sim 10 \text{ kJ mol}^{-1}$  higher than the B97-1 barrier. However, the reaction exothermicity, entrance channel reaction paths, and TS barrier for pre-reaction complex to products are just signatures of the PES, and may only make minor contributions to the dynamics for the high energy 1.53 eV reaction. In inspecting the trajectories, it is found that 55% of the reaction follows an indirect mechanism with B97-1, but only 11% with MP2. Such differences, as well as the  $\sim 4$  times larger reaction cross section with B97-1, most likely result from high energy features of the PES. More work needs to be done to determine which electronic structure theories, and their PES properties, give accurate dynamics for the  $\text{F}^- + \text{CH}_3\text{I} \rightarrow \text{CH}_3\text{F} + \text{I}^-$   $\text{S}_{\text{N}}2$  reaction at both low and high energies. Overall, this work has illustrated the utility of direct dynamics simulations for assessing the accuracy of electronic structure theories and their PESs. Additional studies like the one presented here are important.

## Acknowledgements

The direct dynamics simulations reported here are based upon work supported by the Robert A. Welch Foundation under Grant No. D-0005. Support was also provided by the High-Performance Computing Center (HPCC) at Texas Tech University, under the direction of Philip W. Smith, the Texas Advanced Computing Center (TACC) at the University of Texas, Austin, and the TTU Department of Chemistry & Biochemistry cluster Robinson, whose purchase was funded by the National Science Foundation under the CRIF-MU Grant No. CHE-0840493. The authors wish to acknowledge the Welch Summer Scholar Program which supported the summer research of Collin Davda. Jiaxu Zhang acknowledges the Fundamental Research Funds for the Central Universities, China (AUGA5710012114) for support of his research. The authors also wish to acknowledge important collaborations with the Roland Wester group regarding  $\text{S}_{\text{N}}2$  reaction dynamics.

## References

- C. A. Lieder and J. I. Brauman, *J. Am. Chem. Soc.*, 1974, **96**, 4028–4030.
- W. N. Olmstead and J. I. Brauman, *J. Am. Chem. Soc.*, 1977, **99**, 4219–4228.
- W. L. Hase, *Science*, 1994, **266**, 998–1002.
- G. H. Peslherbe, H. Wang and W. L. Hase, *J. Am. Chem. Soc.*, 1996, **118**, 2257–2266.
- H. Wang and W. L. Hase, *J. Am. Chem. Soc.*, 1997, **119**, 3093–3102.
- M. L. Chabinye, S. L. Craig, C. K. Regan and J. I. Brauman, *Science*, 1998, **279**, 1882–1886.
- J. M. Gonzales, R. S. Cox III, S. T. Brown, W. D. Allen and H. F. Schaefer III, *J. Phys. Chem. A*, 2001, **105**, 11327–11346.
- J. K. Laerdahl and E. Uggerud, *Int. J. Mass Spectrom.*, 2002, **214**, 277–314.
- L. Sun, K. Song and W. L. Hase, *Science*, 2002, **296**, 875–878.
- P. Manikandan, J. Zhang and W. L. Hase, *J. Phys. Chem. A*, 2012, **116**, 3061–3080.
- R. Otto, J. Xie, J. Brox, S. Trippel, M. Stei, T. Best, M. R. Siebert, W. L. Hase and R. Wester, *Faraday Discuss. Chem. Soc.*, 2012, **157**, 41–57.
- J. Zhang and W. L. Hase, *J. Phys. Chem. A*, 2010, **114**, 9635–9643.
- C. M. Aikens, S. P. Webb, R. L. Bell, G. D. Fletcher, M. W. Schmidt and M. S. Gordon, *Theor. Chem. Acc.*, 2003, **110**, 233–253.
- R. G. Parr and Y. Weitao, *Density-Functional Theory of Atoms and Molecules*, Oxford University Press, USA, 1994.
- J. P. Perdew, K. Burke and M. Ernzerhof, *Phys. Rev. Lett.*, 1996, **77**, 3865–3868.
- C. Lee, W. Yang and R. G. Parr, *Phys. Rev.*, 1988, **37**, 785–789.
- F. A. Hamprecht, A. Cohen, D. J. Tozer and N. C. Handy, *J. Chem. Phys.*, 1998, **109**, 6264–6271.
- A. D. Becke, *J. Chem. Phys.*, 1993, **98**, 1372–1377.
- J. Zhang, J. Mikosch, S. Trippel, R. Otto, M. Weidemuller, R. Wester and W. L. Hase, *J. Phys. Chem. Lett.*, 2010, **1**, 2747–2752.
- J. Mikosch, J. Zhang, S. Trippel, C. Eichhorn, R. Otto, R. Sun, W. A. de Jong, M. Weidemuller, W. L. Hase and R. Wester, *J. Am. Chem. Soc.*, 2013, **135**, 4250–4259.
- R. Sun, J. Xie, J. Zhang and W. L. Hase, *Int. J. Mass Spectrom.*, 2014, DOI: 10.1016/j.ijms.2014.04.006.
- K. Raghavachari, G. W. Trucks, J. A. Pople and M. Head-Gordon, *Chem. Phys. Lett.*, 1989, **157**, 479–483.
- W. R. Wadt and P. J. Hay, *J. Phys. Chem.*, 1985, **82**, 284–298.
- T. H. Dunning Jr., *J. Chem. Phys.*, 1989, **90**, 1007–1023.
- D. E. Woon and T. H. Dunning Jr., *J. Chem. Phys.*, 1993, **98**, 1358–1371.
- W. P. Hu and D. G. Truhlar, *J. Phys. Chem.*, 1994, **98**, 1049–1952.
- K. A. Peterson, B. C. Shepler, D. Figgen and H. Stoll, *J. Phys. Chem. A*, 2006, **110**, 13877–13883.
- K. Fukui, *Acc. Chem. Res.*, 1981, **14**, 363–368.
- D. L. Bunker, *J. Chem. Phys.*, 1962, **37**, 393–403.
- R. Sun, K. Park, W. A. de Jong, H. Lischka, T. L. Windus and W. L. Hase, *J. Chem. Phys.*, 2012, **137**, 044305.
- L. Yang, R. Sun and W. L. Hase, *J. Chem. Theory Comput.*, 2011, **7**, 3478–3483.
- W. L. Hase, *J. Phys. Chem.*, 1986, **90**, 365–374.
- U. Lourderaj, K. Park and W. L. Hase, *Int. Rev. Phys. Chem.*, 2008, **27**, 361–403.
- L. Sun and W. L. Hase, *Rev. Comput. Chem.*, 2003, **19**, 79–146.

- 35 M. Paranjothy, R. Sun, Y. Zhuang and W. L. Hase, *Wiley Interdiscip. Rev.: Comput. Mol. Sci.*, 2013, **3**, 296–316.
- 36 A. Szalbo and N. S. Ostlund, *Modern Quantum Chemistry, Introduction to Advanced Electronic Structure Theory*, Dover, New York, 1996.
- 37 U. Lourderaj, R. Sun, C. K. Swapnil, G. L. Barnes, W. A. de Jong, T. L. Windus and W. L. Hase, *Comput. Phys. Commun.*, 2014, **185**, 1074–1080.
- 38 W. L. Hase, R. J. Duchovic, X. Hu, A. Komornicki, K. F. Lim, D. H. Lu, G. H. Peslherbe, S. R. Swamy, S. R. Vande Linde and A. Varandas, *et al.*, *QCPE Bull.*, 1996, **16**, 671.
- 39 X. Hu, W. L. Hase and T. Pirraglia, *J. Comput. Chem.*, 1991, **12**, 1014–1024.
- 40 M. Valiev, E. J. Bylaska, N. Govind, K. Kowalski, T. P. Straatsma, H. J. J. van Dam, D. Wang, J. Nieplocha, E. Apra, T. L. Windus and W. A. de Jong, *Comput. Phys. Commun.*, 2010, **181**, 1477–1489.
- 41 T. Schlick, *Molecular Modeling and Simulation*, Springer, New York, 2000.
- 42 G. H. Peslherbe, H. Wang and W. L. Hase, *Adv. Chem. Phys.*, 1995, **105**, 171–202.
- 43 L. Sun, W. L. Hase and K. Song, *J. Am. Chem. Soc.*, 2001, **123**, 5753–5756.
- 44 W. H. Miller, W. L. Hase and C. L. Darling, *J. Chem. Phys.*, 1989, **91**, 2863–2868.
- 45 K. N. Swamy and W. L. Hase, *J. Phys. Chem.*, 1983, **87**, 4715–4720.
- 46 G. C. Schatz, *J. Chem. Phys.*, 1983, **79**, 5386–5391.
- 47 W. L. Hase and D. G. Buckowski, *J. Comput. Chem.*, 1982, **3**, 335–343.
- 48 D. Lu and W. L. Hase, *J. Chem. Phys.*, 1988, **89**, 6723–6736.
- 49 J. Zhang, U. Lourderaj, R. Sun, J. Mikosch, R. Wester and W. L. Hase, *J. Chem. Phys.*, 2013, **138**, 114309.
- 50 J. Mikosch, S. Trippel, C. Eichhorn, R. Otto, U. Lourderaj, J. Zhang, W. L. Hase, M. Weidemüller and R. Wester, *Science*, 2008, **319**, 183–186.
- 51 Y. J. Cho, S. R. Vande Linde, L. Zhu and W. L. Hase, *J. Chem. Phys.*, 1992, **96**, 8275–8287.
- 52 D. Lu and W. L. Hase, *J. Chem. Phys.*, 1989, **91**, 7490–7497.
- 53 J. Xie, S. C. Kohale, W. L. Hase, S. G. Ard, J. J. Melko, N. S. Shuman and A. A. Viggiano, *J. Phys. Chem. A*, 2013, **117**, 14019–14027.